M_E_M_O

DATE: 25 October 2002

TO: M. T. Kirk and Robert Tregoning

FROM: P. T. Williams and B. R. Bass

SUBJECT: Status Report on Davis-Besse Analyses

The attached Figs. 1-6 provide a summary of the Davis-Besse analyses performed to date under the new Task 9 of JCN Y6533. In Fig. 1, the cladding properties used in the current study are presented: (a) true stress versus true strain and (b) thermal expansion coefficient versus temperature. The remaining figures address a specific sub-task described in the workscope for Task 9.

Sub-task 9.1D requires an estimate for crack driving forces as a function of flaw size and applied membrane stress in cladding. Table 1 shows the Case Matrix developed for this subtask.

Figure 2 depicts the first step carried out in preparation for the *J*-integral analyses, i.e., calculation of an updated estimate of the exposed cladding "footprint" based on the recent "dental mold" cast from the D-B cavity. That footprint area was estimated to be 28.23 in^2. Comparisons of the latest "footprint" statistics with previous ORNL interpretations are given in the table of Fig. 2(b). The newly calculated "footprint" area was used to define a burst disk having the same lateral surface area under load.

Table 2 presents ductile tearing data for three-wire series-arc stainless steel weld overlay cladding published in NUREG/CR-5511 [1]. The ductile-tearing data presented in Table 2 are plotted as a function of temperature in Fig. 3.

Figure 4 presents nine finite-element models developed for this phase of the analysis. Surface-breaking flaws were centrally located in each burst disk with the three relative flaw depths: a/t = 0.5, 0.25, and 0.05. The models for three flaw lengths of 2.0 inches (50.8 mm), 1.0 inch (25.4 mm), and 3/8 in. (9.525 mm) have been developed.

Each model was loaded with an increasing lateral pressure. The resulting *J*-integral loading paths for the nine models are shown in Fig. 5. Figure 5 also presents a value of J_{Ic} for a temperature of 318.3 °C (605 °F) estimated by extrapolating from the data in Fig. 3a using a 4^{th} order polynomial curve-fit.

Figure 6 compares the critical pressures (determined from the results shown in Fig. 5) for two potential failure modes of the burst-disk models. The ductile-tearing critical pressure is calculated from the point at which the load path for each flaw crosses the J_{Ic} line in Fig. 5 and represents the pressure at which stable ductile tearing initiates. The plastic-collapse critical pressure was estimated from the load at which each model began to approach a numerical instability in the analysis. From the curves in Fig. 6, the controlling failure mode for the two larger flaws in the current study was ductile tearing. The shallow flaw (a/t = 0.05) was close to the J_{Ic} line when it began to fail by plastic collapse.

Estimates of the applied tearing modulus shown in Fig. 3b were calculated using the data (see Fig. 5) from the three flaws with $2L$ = 2.0 in. at a pressure of 6.4 MPa (0.928 ksi), three flaws

H 36

with $2L = 1.0$ in. at a pressure of 8.2 MPa (1.19 ksi), and three flaws with $2L = 0.375$ in. at a pressure of 14.93 MPa (2.165 ksi). As indicated by the comparison in Fig. 3b, these estimates of the applied tearing modulus indicate a *stable* ductile tearing for the larger flaws, thus implying *stable* tearing for smaller flaws as well.

References

[1] F. M. Haggag, W. R. Corwin, and R. K. Nanstad, *Irradiation Effects on Strength and Toughness of Three-Wire Series-Arc Stainless Steel Weld Overlay Cladding,* NUREG/CR-5511 (ORNL/TM-11439), Oak Ridge National Laboratory, February 1990.

Table 1. Case Matrix for Task 9.1D

Case Number	a (inches)	$2L$ (inches)	a/t (-)	$2L/a$ (-)
9.1D1	0.1250	2	0.50	16
9.1D2	0.0625	2	0.25	32
9.1D3	0.0125	2	0.05	160
9.1D4	0.1250	1	0.50	8
9.1D5	0.0625	1	0.25	16
9.1D6	0.0125	1	0 05	80
9.1D7	0.1250	0.375	0.50	3
9.1D8	0.0625	0.375	0.25	6
9.1D9	0.0125	0.375	0.05	30

Table 2. Ductile Tearing Data Extracted from Table 13 of NUREG/CR-5511.

Specimen	Test Temperature (°C)	J_{Ic} (kJ/m^2)	Tearing Modulus
Unirradiated Specimens			
A13G	-75	117	64
H2	-75	137	49
A15B[a]	20	165	270
A13D	20	134	209
A10G	20	171	176
A10E	120	128	246
H5	120	119	229
H3	120	120	232
A13F[a]	120	159	359
H6	200	90	240
H4	200	111	231
A15D	288	77	267
A13C	288	66	170
H1	288	82	192
Irradiated Specimens			
A15F	-75	78	40
A15G	-75	56	36
A13A	30	144	177
A15C	50	124	146
A10F	120	94	175
A15A	288	25	191

[a] Specimen was not side-grooved, while all other specimens in table were side-grooved 20%.

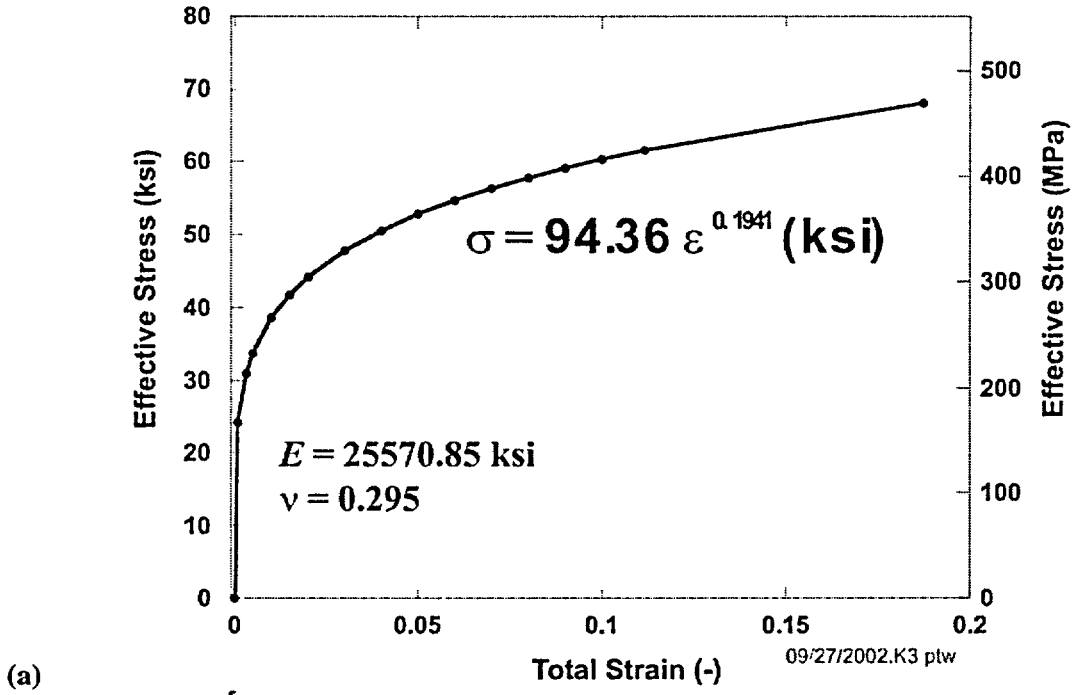

(a)

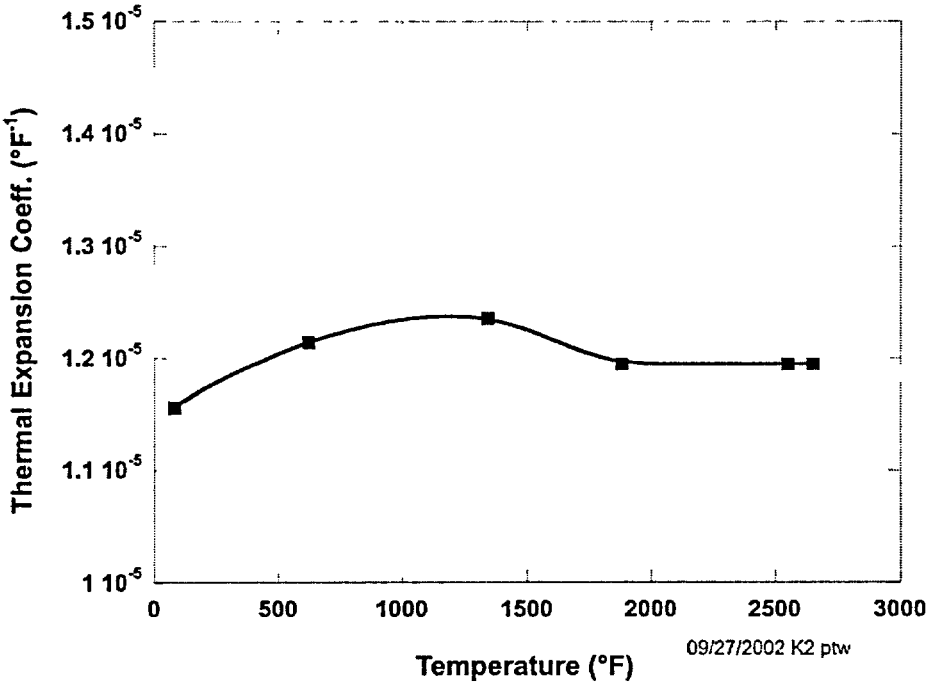

(b)

Fig. 1. Cladding properties used in the current study: (a) true stress vs true strain and (b) thermal expansion coefficient.

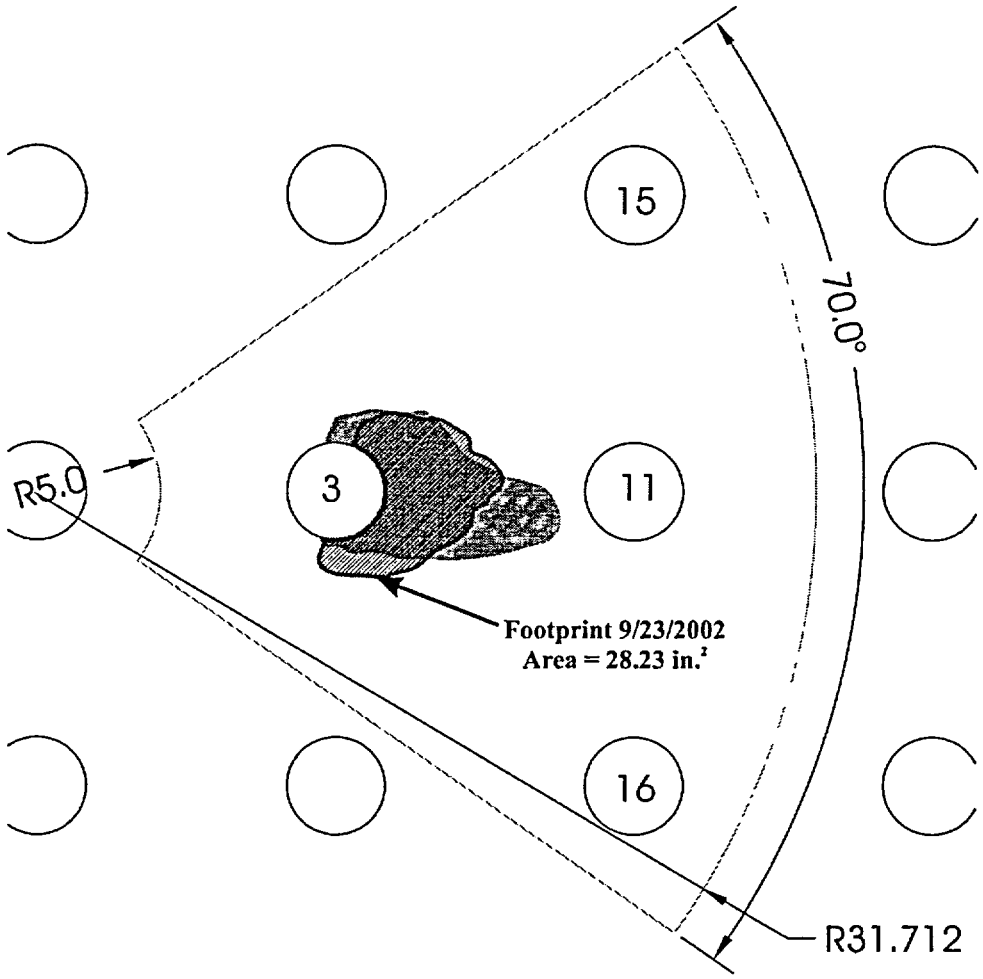

(a)

Description	Scaling Factor	Area	Perimeter	Centroid of Wastage Area Footprint		Moments of Inertia About the Centroid			Eigenvalue Extraction for Principal Moments and Directions			
									Principal Moments		Principal Directions	
		(in^2)	(in.)	(in.)	(in.)	(in^4)	(in^4)	(in^4)	(in^4)	(in^4)	$<n_x, n_y>$	$<n_x, n_y>$
As Found Footprint	1	35.36	30.36	16 4122	-0 1194	98 89	9699 33	-117 16	75 26	197 41	<0 9004, -0 4351>	<0 4351, 0 9004>
Adjusted Footprint for Bounding Calculation	0 25 in.	40 06	31 78	16 4301	-0 1255	129 02	11031 81	-141.35	99 00	245 71	<0 8943, -0 4476>	<0 4476, 0 8943>
As-Found Footprint 9/23/2002	1	28.23	24 55	15.332	-0 18	95.56	6708.63	-50 52	54 01	113 07	[0 558 0 830]	[-0 830 0 558]

Footprint centroid is in global coordinates
Global coordinate system has its z-axis aligned with the vertical centerline of the vessel
The x-y plane of the global coordinate system is a horizontal plane
(b) with the x-axis along the line between the centerlines of Nozzles 3 and 11

Fig. 2. Latest footprint estimated from "dental mold".

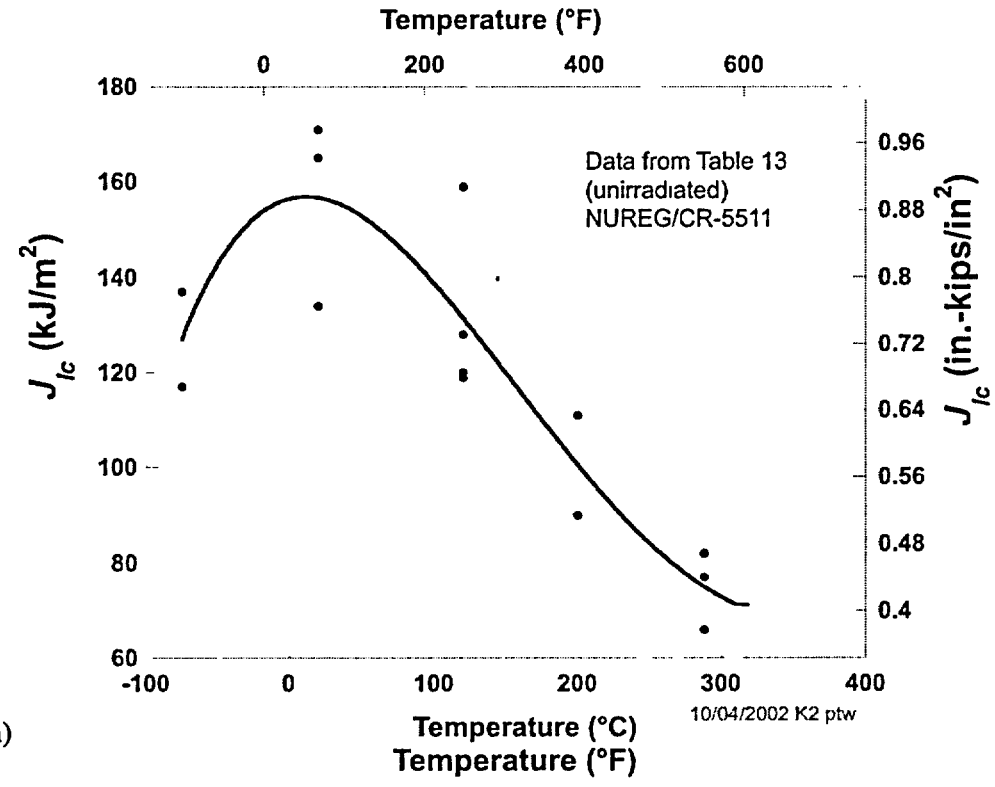

(a)

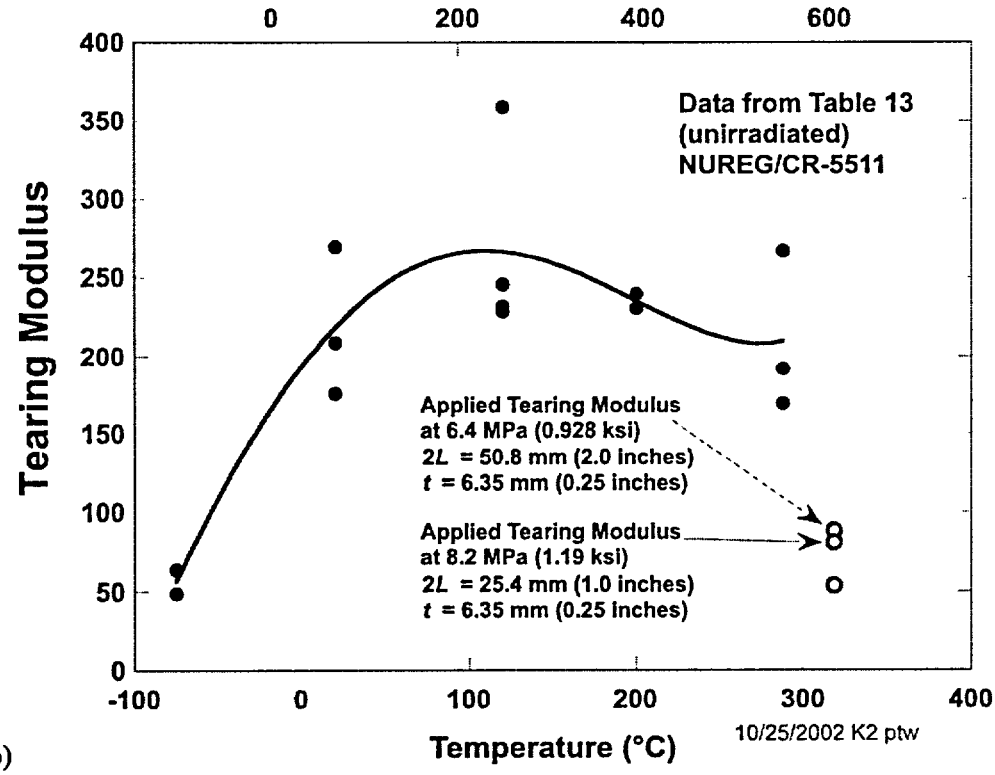

(b)

Fig. 3. Ductile tearing data for three-wire series stainless steel weld overlay cladding from Table 13 of NUREG/CR-5511: (a) J_{Ic} data from unirradiated specimens and (b) tearing modulus data from unirradiated specimens

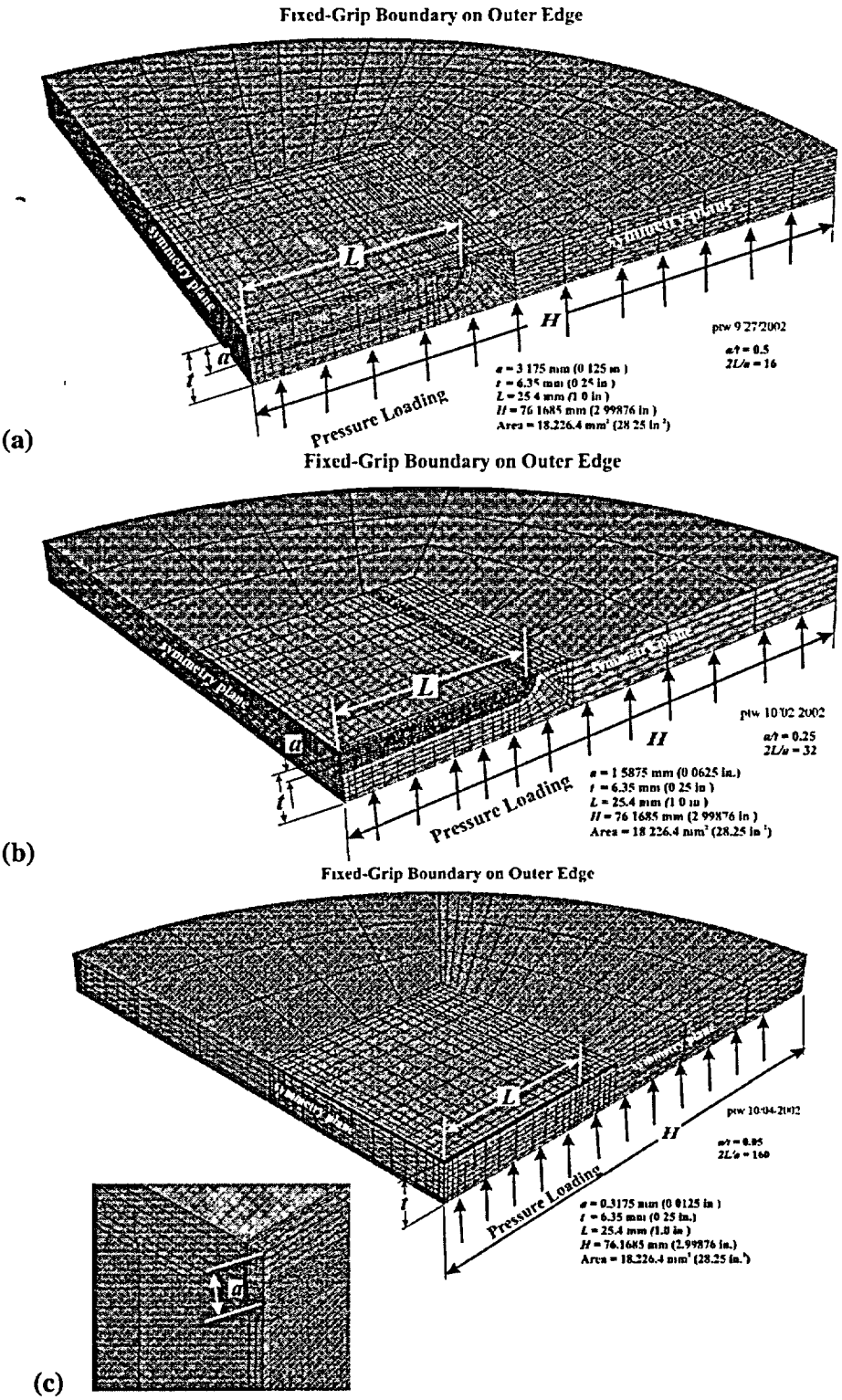

Fig. 4. Finite-element models used in calculating applied *J*-integrals produced by pressure loading of burst disk: (a) Model 9.1D1 ($a/t = 0.5$, $2L/a = 16$) (b) Model 9.1D2 ($a/t = 0.25$, $2L/a = 32$), and (c) Model 9.1D3 ($a/t = 0.05$, $2L/a = 160$) (Task 9.1D)

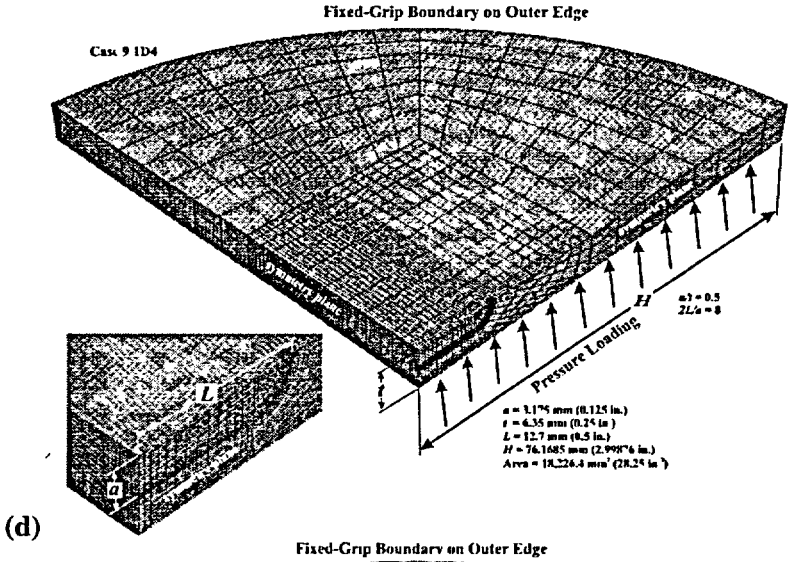

(d)

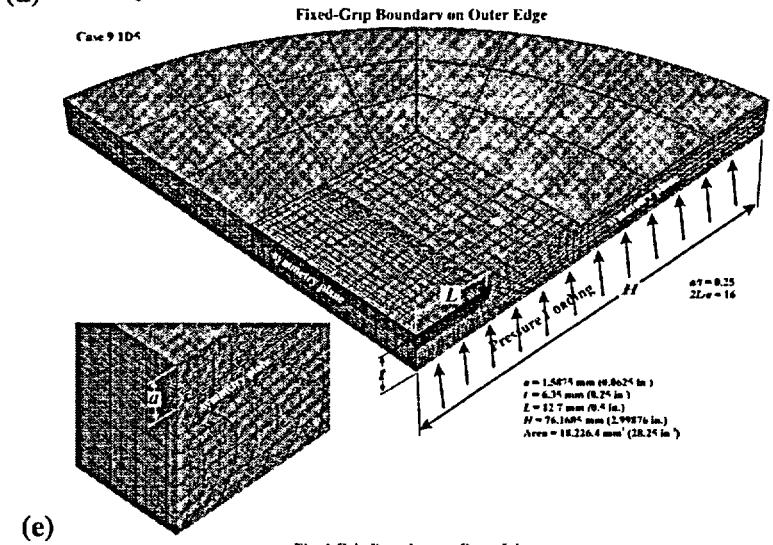

(e)

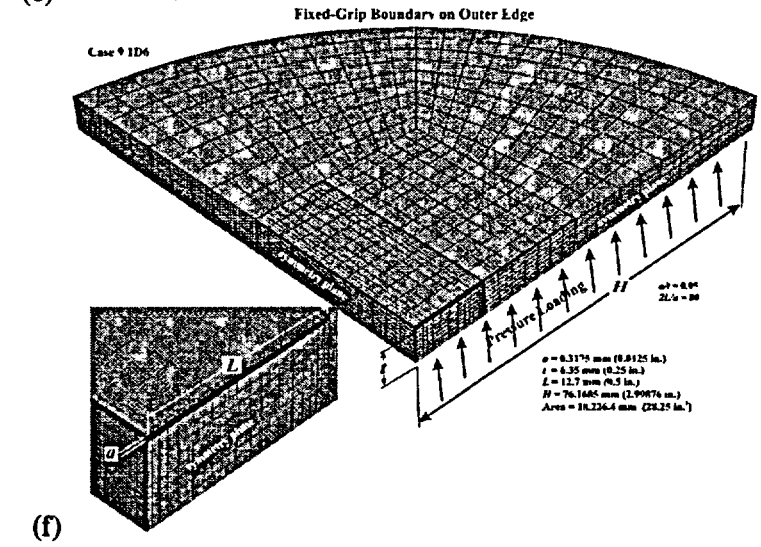

(f)

Fig. 4. (continued) Finite-element models used in calculating applied *J*-integrals produced by pressure loading of burst disk: (d) Model 9.1D4 ($a/t = 0.5$, $2L/a = 8$) (e) Model 9.1D5 ($a/t = 0.25$, $2L/a = 16$), and (f) Model 9.1D6 ($a/t = 0.05$, $2L/a = 80$) (Task 9.1D)

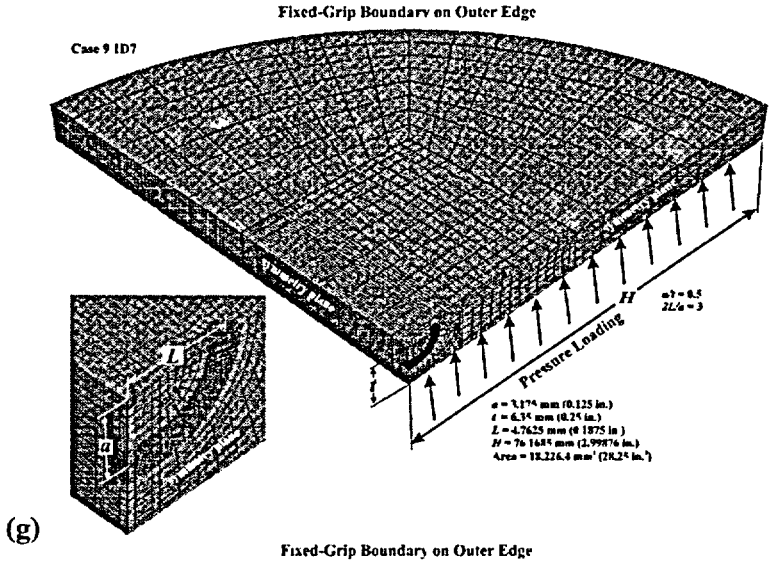

(g)

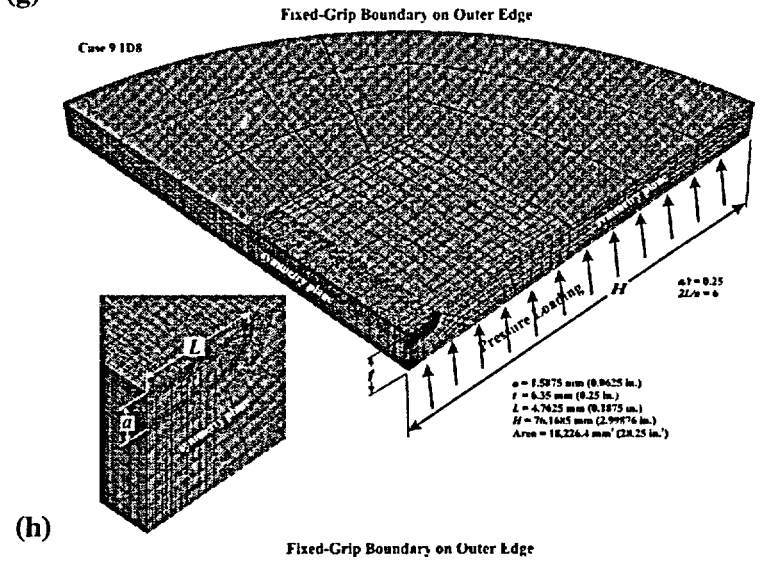

(h)

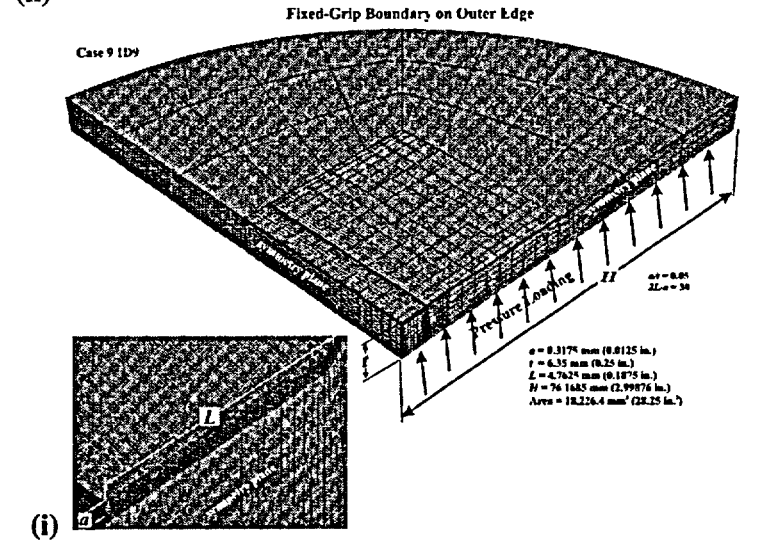

(i)

Fig. 4. (continued) Finite-element models used in calculating applied *J*-integrals produced by pressure loading of burst disk: (g) Model 9.1D7 ($a/t = 0.5$, $2L/a = 3$) (h) Model 9.1D8 ($a/t = 0.25$, $2L/a = 6$), and (i) Model 9.1D9 ($a/t = 0.05$, $2L/a = 30$) (Task 9.1D)

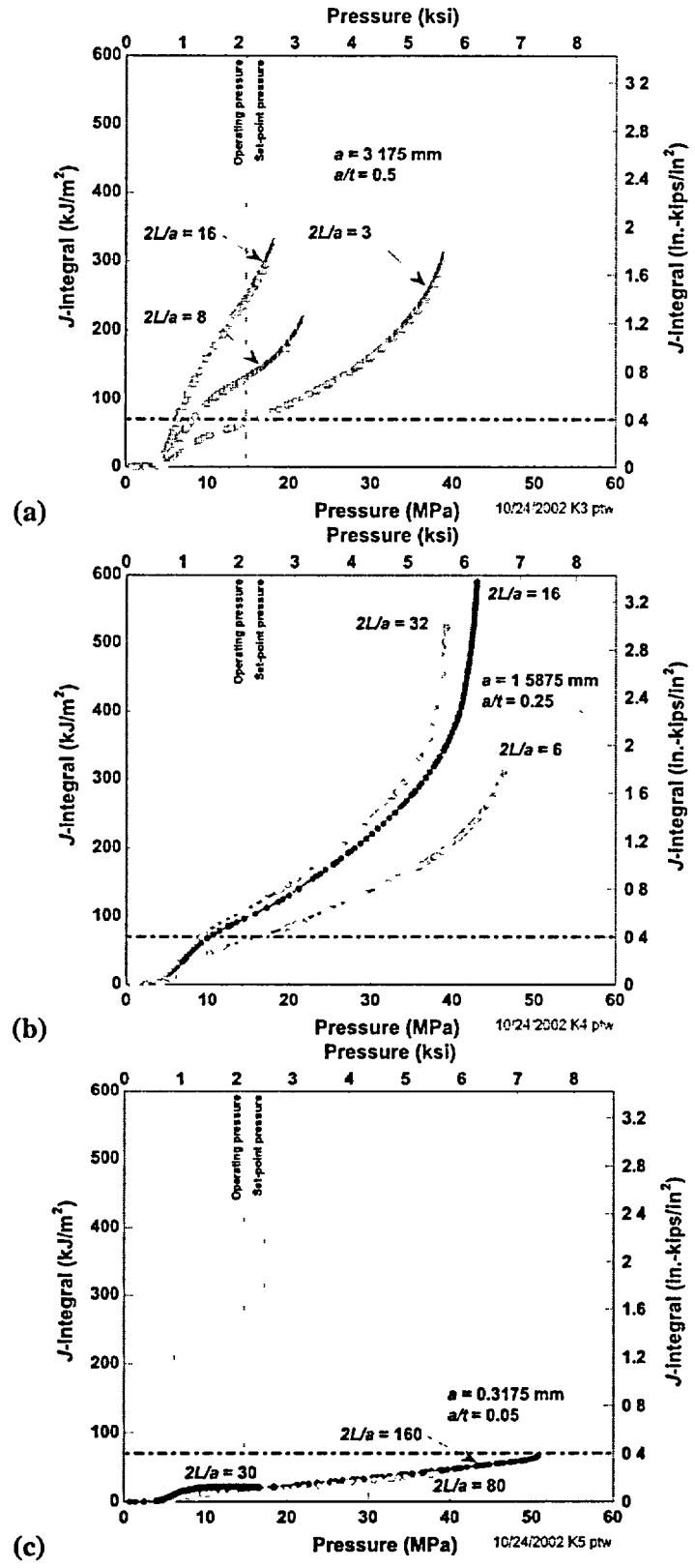

Fig. 5. *J*-integral driving forces from three finite-element models as a function of applied pressure: (a) $a/t = 0.5$, (b) $a/t = 0.25$, and (c) $a/t = 0.05$.

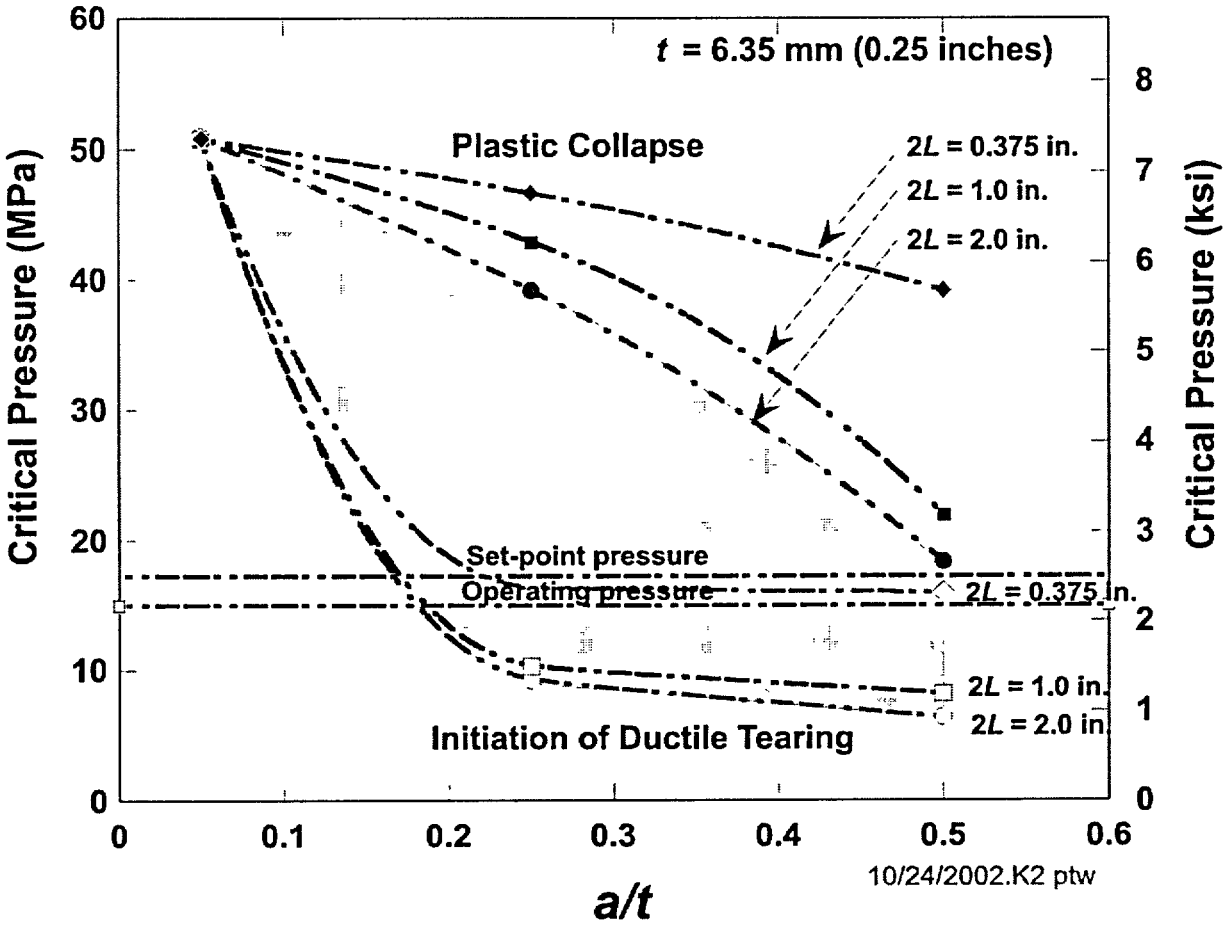

Fig. 6. Comparison of critical pressures for two failure modes as a function of relative flaw depth. Three flaw lengths (2 in. (50.8 mm), 1 in. (25.4 mm), and 3/8 in. (9.525 mm)) were used in the current analysis.